Injection-induced earthquakes on complex fault zones of the Raton Basin illuminated by machine-learning phase picker and dense nodal array

Ruijia Wang[1], Brandon Schmandt[1], Miao Zhang[2], Margaret Glasgow[1], Eric Kiser[3], Sarah Rysanek[1], Ryan Stairs[1]

1. Department of Earth & Planetary Sciences, University of New Mexico, Albuquerque, NM, US
2. Department of Earth and Environmental Sciences, Dalhousie University, Halifax, NS, Canada
3. Department of Geosciences, University of Arizona, Tucson, AZ, US

Corresponding author: ruijia.wang@ualberta.ca

Key points:

1. A machine-learning phase picker and dense nodal array enabled location of ~10,000 earthquakes in a month
2. Hypocenter patterns and moment tensors vary among clusters, unveiling reactivation of complex basement faults
3. Raton Basin seismicity exhibits frequency-magnitude distribution and spatiotemporal evolution comparable to tectonic events

Key words:

Machine-learning; nodal array; induced seismicity; focal mechanism; earthquake detection and location; statistical analysis

Abstract

Seismicity in the Raton Basin over the past two decades suggests reactivation of basement faults due to waste-water injection. In the summer of 2018, 96 short-period three-component nodal instruments were installed in a highly active region of the basin for a month. A machine-learning based phase picker (PhaseNet) was adopted and identified millions of picks, which were associated into events using an automated algorithm – REAL (Rapid Earthquake Association and Location). After hypocenter relocation with hypoDD, the earthquake catalog contains 9259 M_L -2.2 – 3 earthquakes focused at depths of 4-6 km. Magnitude of completeness (Mc) varies from -1 at night to -0.5 in daytime, likely reflecting noise variation modulated by wind. The clustered hypocenters with variable depths and focal mechanisms suggest a complex network of basement faults. Frequency-magnitude statistics and the spatiotemporal evolution of seismicity are comparable to tectonic systems.

Plain Language Summary

Earthquakes induced by waste-water injection are widely observed worldwide and have been occurring in the Raton Basin (located at the border of New Mexico and Colorado) for two decades. We deployed 96 short-period seismic stations in the summer of 2018 to investigate the faults in the southern section of Raton Basin. Earthquake detection was performed with state-of-the-art machine learning techniques, which led to a catalog with ~10,000 earthquakes with magnitude ranging from -2.2 to 3. Clusters of earthquakes were investigated in detail. We found that the orientation of the faults varies within the study region and that induced earthquakes may exhibit spatial-temporal-magnitude clustering just like tectonic ones. Successful application of the automated catalog-building workflow also sheds light on the power of “hands-free” processing of large-volume seismic data.

1. Introduction

Recent M>5 induced earthquakes are mostly associated with fluid injection or extraction such as waste-water injection in Oklahoma, U.S. (e.g., Keranen et al., 2014), geothermal production

in Pohang, Korea (e.g., Grigoli et al., 2018), and hydraulic fracturing or salt mine exploration in Sichuan, China (e.g., Liu, J., & Zahradník, J., 2020; Lei et al., 2019; Meng et al., 2019). In the Raton Basin, waste-water injection related to coal-bed methane production is thought to be the dominant driver of increased seismicity over the past two decades (Rubinstein et al., 2014; Nakai et al., 2017a). Several M_w>4 earthquakes have been reported with normal-faulting focal mechanisms in the Colorado section of the basin (Barnhart et al., 2014). The focal mechanism of the largest earthquake (M_w 5.3), located in the center of the basin, indicated a NE-SW oriented normal fault (Fig. 1), consistent with the linear distribution of its foreshocks and aftershocks (Rubinstein et al., 2014). However, the fault that hosted the M_w 5.3 Trinidad event became quiescent starting in 2012, with more recent seismicity concentrated further west and south in the basin (Fig. 1; USGS, 2020).

Within the southern or New Mexico section of the basin, injection started in 1999 and the average monthly volume is 153,633 m^3 based on publicly available data after 2004 (see Acknowledgement for data resource). The injection wells were drilled 0.15-0.5 km beneath the surface (i.e., above sea level, elevation of the Raton Basin is ~2.5 km) and above the Precambrian basement (depth 1-2 km; Weingarten 2015). Injection is driven by gravity instead of active pumping. Since the injection began, the seismicity rate in the New Mexico section is around five M_L>3 events per year and their hypocenter depths suggest reactivation of basement faults (Rubinstein et al., 2014; Nakai et al., 2017a). Prior studies enabled by the Transportable Array (TA, 2008-2010) and other temporary arrays suggested seismicity clustered in three ~N-S steeply dipping fault zones (Nakai et al., 2017b). However, accurate earthquake detection and location have been challenged by the sparse seismic network within the Raton Basin, preventing more detailed investigation of fluid-fault interactions.

Using a dense nodal array and state-of-the-art programs, we detect 10168 events with M_L-2.2 – 3 and unveil the small-scale faults within the southern section of the Raton Basin. Cluster behaviors are further investigated with moment tensors and statistical analysis. Successful application of the automated catalog-building workflow also sheds light on the power of "hands-free" processing of large-volumes of three-component nodal data.

2. Data and Methods

2.1 Data

Previous seismic monitoring in the Raton Basin relied on the TA network and more distant regional stations. Only one TA station is located within the basin (T25A), near its eastern edge (Fig. 1a). In 2016, seven broadband stations were deployed by the University of New Mexico, three of which provide telemetered data. The USGS uses these telemetered stations for routine catalog detection of earthquakes with M_L >~3 (Fig. 1a). Some double-couple moment tensor solutions are estimated for the M_L>4 earthquakes by Saint Louis University (http://www.eas.slu.edu/eqc/). The USGS catalog and preliminary moment tensor solutions provide first-order information on fault orientations.

The three-component nodal array (96 stations) was deployed between 12 May 2018 and 15 June 2018, in the southern portion of the Raton Basin (Fig. 1). The USGS reported two M_w2.8 earthquakes during the node deployment (USGS, 2020). Inter-station spacing is mostly between 2-5 km, and the nodal array was surrounded by four existing broadband stations (Fig. 1b). The node sampling rate is 250 Hz and the corner frequency of the internal geophones is 5 Hz. The nodes were buried ~10 cm beneath the surface with elevations from 2156 m to 2881 m. For consistency, all station elevations, injection and event depths are presented relative to sea level.

2.2 Earthquake detection and location

An earthquake catalog was built by applying four publicly available packages to three-component raw time series data. First, a machine-learning phase-picker (PhaseNet; Zhu and Beroza, 2019) was used to identify P and S arrivals with confidence levels (i.e., probability). PhaseNet comes with a training dataset that contains 700,000 waveforms with manual picks from northern California over 30 years and includes a mix of instrument types (i.e., from extremely short period to broadband). While the scale of our study area is much smaller than northern California, it is unrealistic to create a new training dataset with a comparable number

of manual picks. We ran PhaseNet with the original nodal sample rate of 250 Hz (12 sec windows; i.e., 3000 data points per window), even though the training dataset is sampled at 100Hz (30 sec windows). Such modification is based on earthquake self-similarity principle (e.g. Shearer, 2012), as the machine-learning algorithm itself does not recognize any absolute time or amplitude scale. In other words, P and S waves for an M_L0 event will be similar to those of a rescaled M_L1. Our test shows that using the 250 Hz data enables detection of twice as many events as using the node data down-sampled to 100 Hz (Fig. S2). Down-sampling mainly diminishes detection of low-magnitude earthquakes. For the 118 events that were visually picked using the nodal array, PhaseNet picks show good agreement with manual picks. The averaged differences between the two picking methods for P and S picks are 0.012 sec and 0.025 sec, respectively (Fig. S3).

The second step of event association used over 5 million P picks and 8 million S picks identified with confidence greater than 0.5 by PhaseNet. These picks were passed to REAL (Zhang et al., 2019) for association and preliminary earthquake location. At this step, a minimum of ten P arrivals, five S arrivals and eighteen total phase arrivals (i.e., P+S) were required for an event detection, with a residual arrival time tolerance of 0.5 sec. Fewer S arrivals are required, based on their lower probability than P picks (see Fig. S3). These requirements are generally stricter than in regional-scale studies with less station coverage (e.g., Liu et al., 2019). The grid searched by REAL covers ~60 km from the center of the array and extends to 15 km depth, with 2 km grid spacing. In total, 10,168 events are detected with station gaps < 270^o (Fig. 2). The third processing step involved absolute location improvement with station corrections in VELEST (Kissling et al., 1995). In the fourth and final step of catalog building, refined hypocenters were obtained with the double-difference relocation algorithm hypoDD (Waldhauser and Ellsworth, 2000), where only picks with confidence greater than 0.75 were used. A consistent 1D velocity model (modified after Rubinstein et al., 2014) was used throughout all hypocenter estimation steps (Fig. S1).

The final relocated catalog contains 9259 earthquakes, 91% of the initial detections from REAL, showing consistent but much more detailed fault patterns than previously available catalogs

(e.g., USGS). Events that did not make the last round appear more randomly distributed (Fig. 2a). The high survival rate and consistent location patterns suggest that our sequential workflow shows promising potential for building a robust catalog from the dense nodal array.

2.3 Magnitude calculation

We calculated local magnitude (M_L) from the displacement waveforms in a way similar to the classic method (Gutenberg and Ritchter,1956). After removing instrument response and filtering from 1- 125 Hz, three-component waveforms are cut from 0.5 sec before the P arrival and 3 sec after S arrival of an earthquake. The peak amplitude (A) is calculated from the square root of three component energy within an event window. A distance correction (unit km) is also added without normalization (i.e., 100 km), as our largest event-station distance is ~40 km.

$$M_L = \log 10(A) + 2.56 \log 10(dist) - 1.17$$

The calculation is performed at each station that has at least one arrival (P or S). The number of stations used ranges from 10 to 96, with an average of 25. The final M_L of an earthquake is then determined from the median value of all single-station M_L (Fig. S3). The magnitude-frequency distribution of the final catalog follows the Gutenberg-Richter law with a b-value close to 1 (Fig.3a).

A strong diurnal variation is observed after magnitude calculation (Fig. 2b). The magnitude of completeness, Mc, varies from -1 at night to -0.5 during local daytime hours (Fig. 3a). Access to the area of the node array is restricted by gates and road traffic is sparse during normal operations. There was no new drilling or major construction activity during the nodal deployment and most of the area is managed for wildlife conservation. Consequently, we considered potential natural sources of high-frequency diurnal noise variations. A likely contributor is identified by comparing hourly wind-speed (averaged over the month) with hourly earthquake detections. They are anti-correlated with a correlation-coefficient of -0.77 (Fig. 3b). Wind effects on high-frequency background noise (>1 Hz) of surface sensors are expected for wind speeds as low as 3 m/sec (6.7 mph; Withers et al., 1996) and such strong wind was commonly present in the Raton Basin from mid-day to early evening during the node

deployment (Fig. 3b). Other possibilities that are less favored or difficult to assess with only 1 month of data are discussed in the supplementary material (Fig. S4-S6).

2.4 Moment tensor estimation

We inverted four moment tensors in the time-domain using TDMT_INV (Dreger, 2003) and three-component waveforms recorded by the broadband stations (network YX and T25A). Three out of four events occurred during the node deployment and their hypocenter locations are better located (i.e., uncertainty < 0.5 km, compared to USGS catalog). The fourth event is adopted to reveal the NW-SE normal fault structure of cluster 1 based on the USGS reported location. Parameter details are provided in the supporting information and also documented in prior work on induced earthquakes in Canada (e.g., Wang et al., 2016). In this case, we limit the inversion for deviatoric components only, considering the relatively low signal-to-noise ratio for M<3 earthquakes at low frequency (waveform fits are shown in Fig. S7-9). The faulting parameters (i.e., strike, rake, dip) are within 5° difference of an independent high-frequency first motion analysis using the nodal array (Table S2).

3. Discussion

3.1 Fault structures and sub-cluster behaviors

The dense nodal array and machine-learning based phase picker exposes reactivated fault zone structures in the Raton Basin in only one month. The new catalog shows four distinct clusters (Fig. 4a): 1) the NW cluster within the Colorado section that exhibits NW-SE fault orientation (28.5% of total detections); 2) the center cluster showing an oblique faulting regime (14.3%); 3) the southern cluster exhibits NNE-SSW normal faulting (54.6%); 4) the deep tight SW cluster that has relatively few hypocenters and lacks a focal solution (0.6%). Among them, clusters 2 and 3 are located beneath the nodal array (Fig. 2a and Fig. 4a), thus their hypocenters are better constrained and discussed in detail.

Cluster 2 hosted the second largest event (M_w2.9, 10 June 2018) during the nodal operation period and has a moderate number of detections (14.3%). To our knowledge, cluster 2 has not

been distinctly identified in previous studies, possibly because the spatial resolution was insufficient to differentiate it from clusters 1 or 3 (Fig.4a). The closest injection well (well ID VPR042) is located within 2 km at a depth of -2 km (above sea level). Differing from any previously identified normal faults (e.g., Rubinstein et al., 2014), the mainshock of this cluster shows dip-slip/strike-slip faulting regime around a depth of 6 km. Despite a well-resolved moment tensor, the spatial distribution of this cluster supports the possibility of slip along either potential fault planes. Future studies of rupture directivity may resolve the ambiguity.

Cluster 3 produced the largest earthquake within the month as well as the most detections (54.6%). Two consistent moment tensors are resolved from the M_w3, 20 May 2018 event and its M_w2.8 aftershock, showing NNE-SSW normal faults. In general, both the focal mechanisms and the hypocenter distribution of cluster 3 are comparable to previous studies (Rubinstein et al., 2014; Barnhart et al. 2014), confirming the ~N-S alignment of the Vermejo Park fault. Moment tensor analysis indicates a strike of 14 degrees toward the east, which coincides with the angle estimated from the epicenters (Fig. 4a). During the month of the nodal deployment, this fault zone was consistently active, with an average rate of ~15 M_L>0 events per day. Our results indicate that the majority of the seismicity occurred on the east segment of this fault zone. Interestingly, the centroid of the largest cluster is ~10 km from the nearest injection wells.

All the clusters are located within the crystalline basement and likely to be induced by waste-water disposal based on the dramatically increased rate of M_L>3 earthquakes since injection began (Rubinstein et al., 2014). Prior research suggested that permeable fault zones allow pore-pressure migration from the injection unit into the basement (Nakai et al., 2017a). Unlike hydraulic-fracturing induced earthquakes that correspond to single well pad within short temporal lags (Schultz & Wang, 2020; Schultz et al., 2018; Rubinstein & Mahani, 2015), waste-water disposal induced events are usually the commutative product of multiple wells over years of injection. Thus, we cannot link any of the identified clusters to a specific injection well. Compared to other areas in the central U.S., the injection wells in the Raton Basin are relatively shallow, ranging from 0.16 km to 0.5 km beneath the surface. An outstanding question is: are the basement faults delineated by hypocenters hydraulically connected to shallower injection?

If the basement faults identified here project upward across the sediment-basement boundary they could serve as fluid pathways; however, even with Mc<0, we do not find clustered hypocenters extending to such shallow depths. If the injection wells are not hydraulically connected to the reactivated basement faults, poroelastic effects of injection can induce the seismicity (e.g., Goebel and Brodsky et al., 2018; Zhai et al., 2018). The variable faulting regimes among the four fault clusters may be related to rotation of the maximum compressive stress orientation from ~N-S to ~NW-SE near the Colorado-New Mexico border (Snee & Zoback, 2020), but the North America stress map does not enable detailed comparison at the scale of the node array.

3.2 Statistical similarity to tectonic earthquake sequences

The large number of events within the two well-constrained clusters (2 and 3) enables further statistical analysis. The first parameter considered is the b-value of the frequency-magnitude distribution, which is ~1 for tectonic earthquakes. For injection-induced events, the b-value has been suggested to vary over time and may reflect the influence of evolving pore-pressure (e.g., Lei et al., 2013). In other cases, magnitude jumps (Schultz & Wang 2020; Igonin et al, 2018) and/or aftershock deficiency (Goebel et al., 2019) are observed, leading to apparently lower b-values. Regardless of the time of day (which affects Mc), cluster location, and depth, we obtained consistent b-values (0.9-1.2) comparable to tectonic earthquakes (i.e., around 1; El-Isa, Z. H., & Eaton, 2014). The second parameter considered is inter-event time, quantified by the coefficient of variation (Cv; Cochran et al., 2018). Low Cv (<1) indicates less clustering and high Cv (>4) suggests tight clustering in time. In our case, clusters 1-3 exhibit moderate clustering in time, with Cv values around 2 (Fig. S10). This uniform neutral clustering observed in the Raton Basin is different from the large variations (i.e., Cv ranging from ~1-7) among waste-water induced seismicity clusters in southern Kansas (Cochran et al., 2018) and the low clustering in northern Oklahoma (Cochran et al., 2020). The third metric, the ETAS modelling (Epidemic Type of Aftershock Sequence; Ogata, 1988), accounts for both event-time and magnitude and shows aftershock-dominated rate increases that are comparable between

cluster 2 and cluster 3. Such seismicity rate increases dominated by the mainshock are similar to tectonic earthquake sequences (Fig. S10).

Next, we examined the nearest-neighbor distances in the space-time-magnitude domain for clusters 2 and 3 (Zaliaplin and Ben Zion, 2013). Taking a b-value of 1, Mc of -0.5, and assuming a modest fractal dimension (i.e., df) of 1.6, both clusters are tightly distributed in rescaled time and space (Fig. 4 c&e). The tight clustering may be unexpected for induced seismicity, as other studies at comparable scales show stationary background seismicity governed by injection (e.g., Vasylkivska & Huerta, 2017; Schoenball et al., 2015; Langenbruch et al., 2011). The only potential divergence from tectonic earthquake behavior is observed from cluster 2, where the rescaled time-space plot shows a weak trend separated by the diagonal in Fig. 4c.

Overall, robust estimation and timely measurements of b-value (and other statistical parameters) are crucial for seismic hazard evaluation because they provide quantitative insight into the evolution of earthquake sequences. Interestingly, our high-resolution one-month catalog shows no significant differences from the statistical behavior of tectonic earthquakes. It is worth noting that this similarity does not contradict the suggested injection-induced nature of seismicity in the Raton Basin, which has been investigated by previous studies (e.g., Rubinstein et al., 2014). Our results highlight the possibility that, in at least some areas, induced seismicity follows the scaling relationships known from tectonic earthquakes, thus traditional methods for hazard assessment and mitigation may be applicable (e.g., Atkinson & Assatourians, 2017). We speculate that the origin of the observed similarity is: the Raton Basin earthquakes are dominantly releasing accumulations of tectonic stress created over geologic time scales.

4. Conclusions

Taking advantage of a machine-learning phase picker and dense nodal array, we detected earthquakes spanning 5 magnitude units in just one month in the Raton Basin.

- The resulting catalog of ~10,000 earthquakes unveils the detailed structure of reactivated basement faults in the southern Raton Basin: The center sub-cluster (2) exhibits a potential dip-slip and/or strike-slip faulting regime, different from the NW-SE normal fault toward the north (1) and NNE-SSW normal fault to the south (3).
- The Mc decrease ~0.5 at night is likely modulated by wind speed.
- Seismicity shows b-values and after-shock clustering in space and time comparable to tectonic events.

The source parameters and statistics presented in this study could benefit regional seismic hazard estimation and physical modelling to understand fluid-fault interactions. This study also demonstrates the capability of machine-learning workflows for efficient assessment of seismogenic structures with dense nodal arrays.

Acknowledgement

The Vermejo Park Ranch, especially staff member Sara Holm, facilitated land access. Justin Wilgus collected the well injection data, which can be accessed from The Oil Conservation Division of the New Mexico Energy Minerals and Natural Resources Department). Nodal array waveform data are available at IRIS DMC under network code 4E (https://doi.org/10.7914/SN/4E_2018) and YX (https://doi.org/10.7914/SN/YX_2016) for the nodal and broadband arrays, respectively. The catalog will be available at ISC upon publication (http://www.isc.ac.uk/iscbulletin/search/catalogue/). The PhaseNet package is available at https://github.com/wayneweiqiang/PhaseNet. The REAL package is available at https://github.com/Dal-mzhang/REAL. The VELEST code is available at https://seg.ethz.ch/software/velest.html. The hypoDD package is available at https://www.ldeo.columbia.edu/~felixw/hypoDD.html. Wind records of the Raton Basin are obtained from https://mesowest.utah.edu/. All links are last accessed in February 2020. Most of the figures are produced with MATLAB and Fig. 1a was created with GMT (Wessel, P., & Smith, 1991) and Google Map Pro. This research was supported by NSF EAR-1554908.

References

Atkinson, G. M., & Assatourians, K. (2017). Are ground-motion models derived from natural events applicable to the estimation of expected motions for induced earthquakes?. Seismological Research Letters, 88(2A), 430-441.

Barnhart, W. D., Benz, H. M., Hayes, G. P., Rubinstein, J. L., & Bergman, E. (2014). Seismological and geodetic constraints on the 2011 Mw5. 3 Trinidad, Colorado earthquake and induced deformation in the Raton Basin. Journal of Geophysical Research: Solid Earth, 119(10), 7923-7933.

Brocher, T. M. (2005). Empirical relations between elastic wavespeeds and density in the Earth's crust. Bulletin of the seismological Society of America, 95(6), 2081-2092.

Cochran, E. S., Ross, Z. E., Harrington, R. M., Dougherty, S. L., & Rubinstein, J. L. (2018). Induced earthquake families reveal distinctive evolutionary patterns near disposal wells. Journal of Geophysical Research: Solid Earth, 123(9), 8045-8055.

Cochran, E. S., Wickham-Piotrowski, A., Kemna, K., Harington, R., Dougherty, S., & Castro., A. P., (2020) Minimal Clustering of Injection-Induced Earthquakes Observed with a Large-n Seismic Array. Bulletin of the Seismological Society of America, in press.

Diaz, J., Schimmel, M., Ruiz, M., & Carbonell, R. (2020). Seismometers within cities: a tool to connect Earth Sciences and society. Frontiers in Earth Science, 8, 9.

Dreger, D. S. (2003). TDMT_INV: Time domain seismic moment tensor inversion. In International Geophysics (Vol. 81, p. 1627). Academic Press.

El-Isa, Z. H., & Eaton, D. W. (2014). Spatiotemporal variations in the b-value of earthquake magnitude–frequency distributions: Classification and causes. Tectonophysics, 615, 1-11.

Goebel, T. H., & Brodsky, E. E. (2018). The spatial footprint of injection wells in a global compilation of induced earthquake sequences. Science, 361(6405), 899-904.

Goebel, T. H. W., Rosson, Z., Brodsky, E. E., & Walter, J. I. (2019). Aftershock deficiency of induced earthquake sequences during rapid mitigation efforts in Oklahoma. Earth and Planetary Science Letters, 522, 135-143.

Grigoli, F., Cesca, S., Rinaldi, A. P., Manconi, A., Lopez-Comino, J. A., Clinton, J. F., ... & Wiemer, S. (2018). The November 2017 Mw 5.5 Pohang earthquake: A possible case of induced seismicity in South Korea. Science, 360(6392), 1003-1006.

Gutenberg, B., and C. F. Richter (1956). Earthquake magnitude, intensity, energy, and acceleration, Bull. Seismol. Soc. Am. 46, 105–145.

Huang, Y., Ellsworth, W. L., & Beroza, G. C. (2017). Stress drops of induced and tectonic earthquakes in the central United States are indistinguishable. Science Advances, 3(8), e1700772.

Heaton, T. H. (1975). Tidal triggering of earthquakes. Geophysical Journal International, 43(2), 307-326.

Keranen, K. M., Weingarten, M., Abers, G. A., Bekins, B. A., & Ge, S. (2014). Sharp increase in central Oklahoma seismicity since 2008 induced by massive wastewater injection. Science, 345(6195), 448-451.

Kissling, E., Kradolfer, U., & Maurer, H. (1995). Program VELEST user's guide-Short Introduction. Institute of Geophysics, ETH Zurich.

Langenbruch, C., Dinske, C., & Shapiro, S. A. (2011). Inter event times of fluid induced earthquakes suggest their Poisson nature. Geophysical Research Letters, 38(21).

Lei, X., Wang, Z., & Su, J. (2019). The December 2018 ML 5.7 and January 2019 ML 5.3 earthquakes in south Sichuan basin induced by shale gas hydraulic fracturing. Seismological Research Letters, 90(3), 1099-1110.

Lei, X., Ma, S., Chen, W., Pang, C., Zeng, J., & Jiang, B. (2013). A detailed view of the injection-induced seismicity in a natural gas reservoir in Zigong, southwestern Sichuan Basin, China. Journal of Geophysical Research: Solid Earth, 118(8), 4296-4311.

Liu, J., & Zahradník, J. (2020). The 2019 MW 5.7 Changning earthquake, Sichuan Basin, China–a shallow doublet with different faulting styles. Geophysical Research Letters, e2019GL085408.

Liu, M., Zhang, M., Zhu, W., Ellsworth, W. L., & Li, H. (2020). Rapid Characterization of the July 2019 Ridgecrest, California Earthquake Sequence from Raw Seismic Data using Machine Learning Phase Picker. Geophysical Research Letters, e2019GL086189.

Meng, L., McGarr, A., Zhou, L., & Zang, Y. (2019). An investigation of seismicity induced by hydraulic fracturing in the Sichuan basin of China based on data from a temporary seismic network. Bulletin of the Seismological Society of America, 109(1), 348-357.

Nakai, J. S., Weingarten, M., Sheehan, A. F., Bilek, S. L., & Ge, S. (2017a). A possible causative mechanism of Raton Basin, New Mexico and Colorado earthquakes using recent seismicity patterns and pore pressure modeling. Journal of Geophysical Research: Solid Earth, 122(10), 8051-8065.

Nakai, J. S., A. F. Sheehan, and S. L. Bilek. (2017b). Seismicity of the Rocky Mountains and Rio Grande Rift from the EarthScope Transportable Array and CREST temporary seismic networks, 2008-2010." Journal of Geophysical Research: Solid Earth 122.3, 2173-2192.

354 Ogata, Y. (1988). Statistical models for earthquake occurrences and residual analysis for point
355 processes. Journal of the American Statistical association, 83(401), 9-27.

356 Shearer, P. M. (2012). Self-similar earthquake triggering, Båth's law, and foreshock/aftershock
357 magnitudes: Simulations, theory, and results for southern California. Journal of Geophysical
358 Research: Solid Earth, 117(B6).

359 Rubinstein, J. L., Ellsworth, W. L., McGarr, A., & Benz, H. M. (2014). The 2001–present induced
360 earthquake sequence in the Raton Basin of northern New Mexico and southern Colorado.
361 Bulletin of the Seismological Society of America, 104(5), 2162-2181.

362 Rubinstein, J. L., & Mahani, A. B. (2015). Myths and facts on wastewater injection, hydraulic
363 fracturing, enhanced oil recovery, and induced seismicity. Seismological Research Letters, 86(4),
364 1060-1067.

365 Schmandt, B., Lin, F. C., & Karlstrom, K. E. (2015). Distinct crustal isostasy trends east and west
366 of the Rocky Mountain Front. Geophysical Research Letters, 42(23), 10-290.

367 Schoenball, M., Davatzes, N. C., & Glen, J. M. (2015). Differentiating induced and natural
368 seismicity using space-time-magnitude statistics applied to the Coso Geothermal field.
369 Geophysical Research Letters, 42(15), 6221-6228.

370 Schultz, R., Wang, R., Gu, Y. J., Haug, K., & Atkinson, G. (2017). A seismological overview of the
371 induced earthquakes in the Duvernay play near Fox Creek, Alberta. Journal of Geophysical
372 Research: Solid Earth, 122(1), 492-505.

373 Schultz, R., & Wang, R. (2020). Newly emerging cases of hydraulic fracturing induced seismicity
374 in the Duvernay East Shale Basin. Techtonophysics.

375 Snee, J. E. L., & Zoback, M. D. (2020). Multiscale variations of the crustal stress field throughout
376 North America. Nature Communications, 11(1), 1-9.

377 USGS (2020). ANSS comprehensive earthquake catalog (ComCat).

378 Vasylkivska, V. S., & Huerta, N. J. (2017). Spatiotemporal distribution of Oklahoma earthquakes:
379 Exploring relationships using a nearest-neighbor approach. Journal of Geophysical Research:
380 Solid Earth, 122(7), 5395-5416.

381 Waldhauser, F., & Ellsworth, W. L. (2000). A Double-Difference Earthquake Location Algorithm:
382 Method and Application to the Northern Hayward Fault, California. BSSA, 90, 1353-1368.Wang,
383 R., Gu, Y. J., Schultz, R., Kim, A., & Atkinson, G. (2016). Source analysis of a potential hydraulic-
384 fracturing-induced earthquake near Fox Creek, Alberta. Geophysical Research Letters, 43(2),
385 564-573.

386 Wang, R., Gu, Y. J., Schultz, R., & Chen, Y. (2018). Faults and non-double-couple components for
387 induced earthquakes. Geophysical Research Letters, 45(17), 8966-8975.

Weingarten, M. B. (2015). On the interaction between fluids and earthquakes in both natural and induced seismicity.

Wessel, P., & Smith, W. H. (1991). Free software helps map and display data. Eos, Transactions American Geophysical Union, 72(41), 441-446.

Wiemer, S. (2001). A software package to analyze seismicity: ZMAP. Seismological Research Letters, 72(3), 373-382.

Withers, M. M., Aster, R. C., Young, C. J., & Chael, E. P. (1996). High-frequency analysis of seismic background noise as a function of wind speed and shallow depth. Bulletin of the Seismological Society of America, 86(5), 1507-1515.

Zhang, M., Ellsworth, W. L., & Beroza, G. C. (2019). Rapid Earthquake Association and Location. Seismological Research Letters, 90(6), 2276-2284.

Zaliapin, I., & Ben-Zion, Y. (2013). Earthquake clusters in southern California I: Identification and stability. Journal of Geophysical Research: Solid Earth, 118(6), 2847-2864.

Zhai, G., Shirzaei, M., Manga, M., & Chen, X. (2019). Pore-pressure diffusion, enhanced by poroelastic stresses, controls induced seismicity in Oklahoma. Proceedings of the National Academy of Sciences, 116(33), 16228-16233.

Zhu, W., & Beroza, G. C. (2019). PhaseNet: a deep-neural-network-based seismic arrival-time picking method. Geophysical Journal International, 216(1), 261-273.

Figures

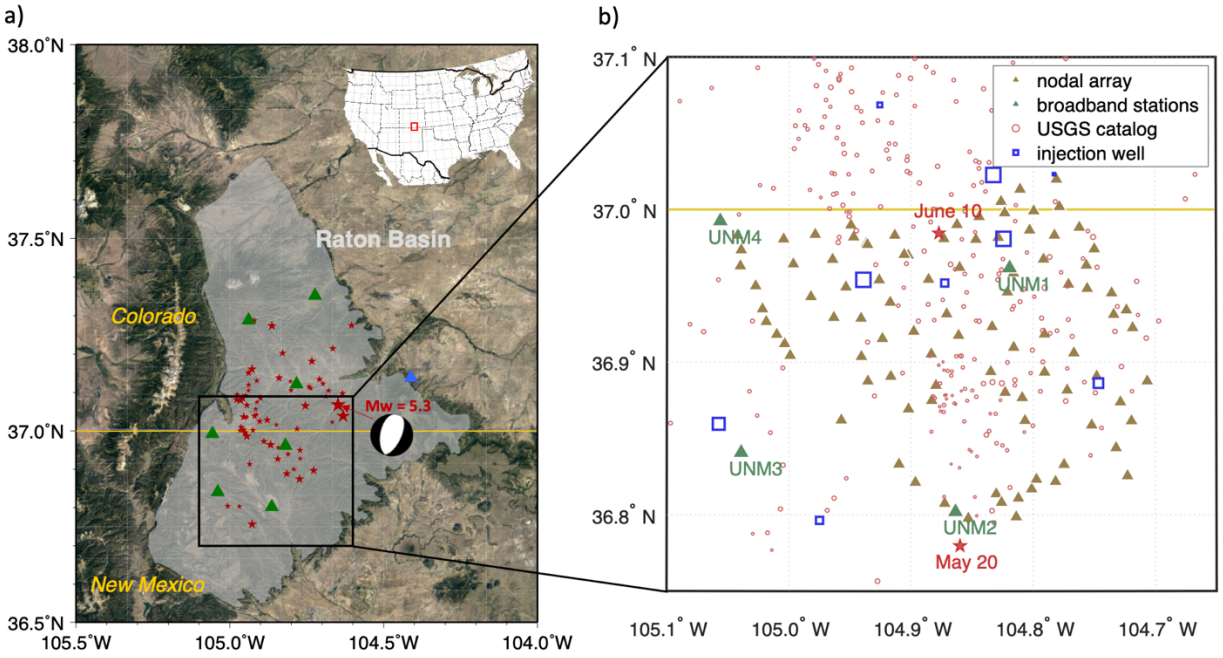

Figure 1. Map of study area. a) The Raton Basin region and USGS reported M_L>3 earthquakes since 1992 (red stars), along with existing broadband stations (green triangles - UNM1-7, 2016-present; blue triangle - T25A, 2008-present). The "beachball" represents the focal mechanism of the 2011 M_w 5.3 Trinidad, Colorado earthquake (Rubinstein et al., 2014). (Inset) Regional map of the U.S., with the red rectangle indicating the study region. b) Zoomed-in area in figure a. Red stars mark two M_w~3 events during the nodal deployment period. The sizes of the injection wells are scaled with average monthly injection volume (largest symbol representing 266,667m^3/month) over the five-year (2013-2018) period before nodal deployment.

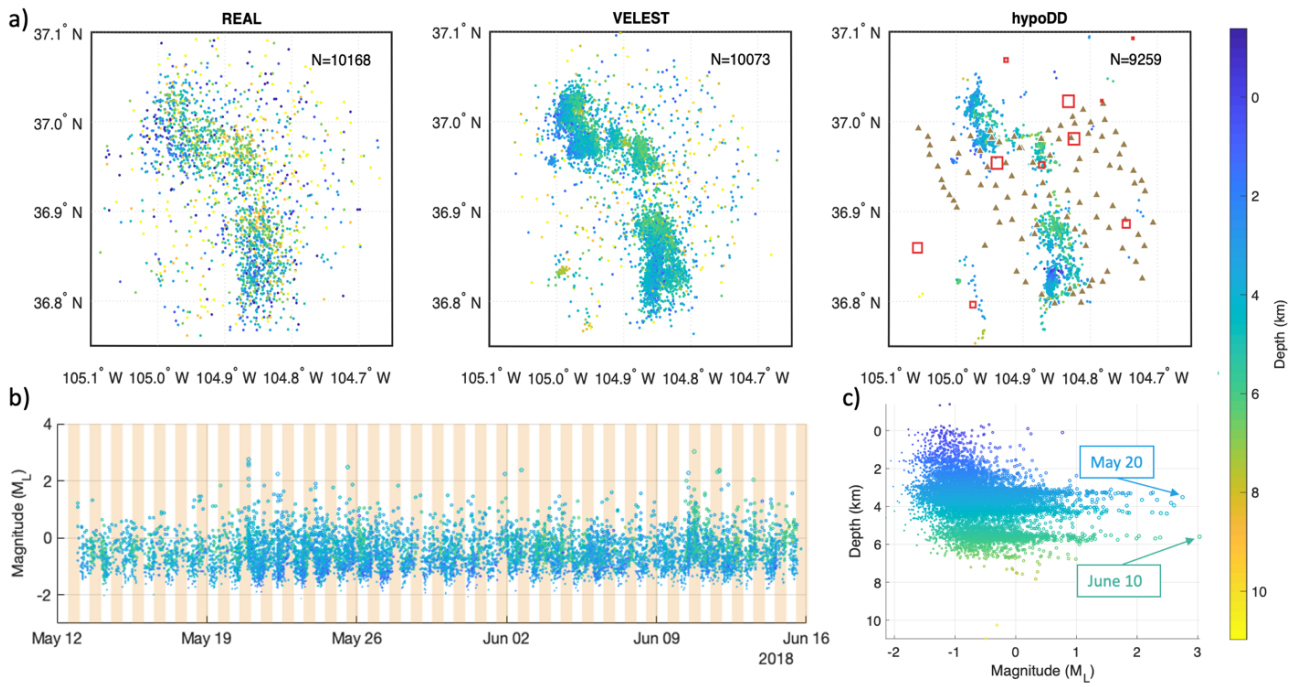

Figure 2. Spatial distribution and magnitudes of seismicity. a) Detections at each step of catalog development. Wells (red squares) and nodal stations (brown triangles) are the same as in Figure1b. b) Event magnitude over time (catalog after hypoDD relocation); daytime hours are shaded in light orange. c) Magnitude vs. depth. Color in all figures corresponds to depth (relative to sea-level; see colorbar).

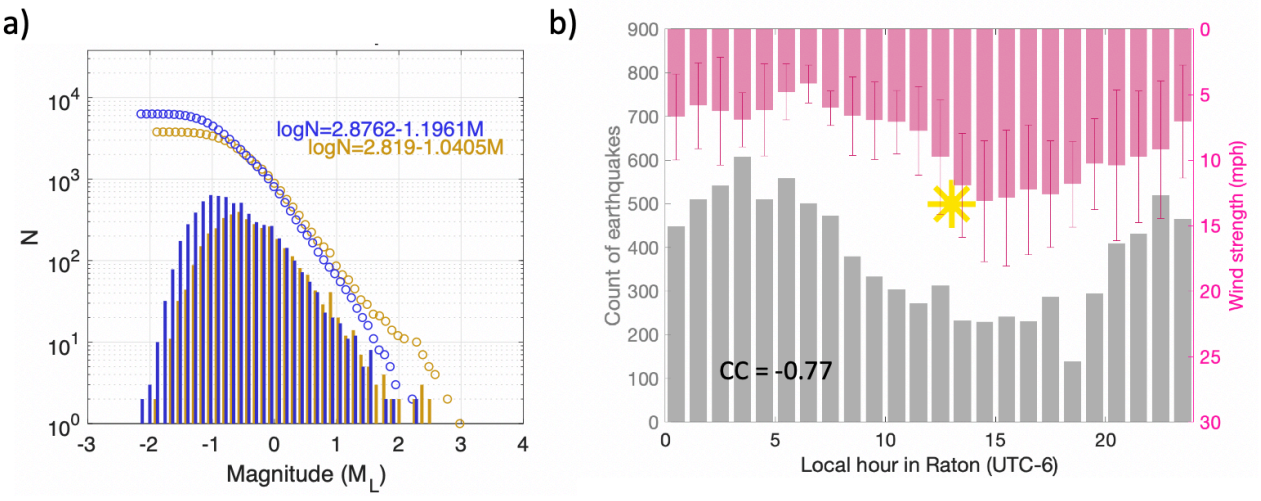

424

425 **Figure 3.** Magnitude of completeness and the relationship between hourly detections and
426 hourly wind speed. a) Gutenberg-Richter law for events during day (yellow) and night (blue). b)
427 Hourly event detection number is anti-correlated with hourly wind speed (pink, Table S1)
428 Detection number and wind strength are averaged hourly over 33 days (i.e., nodal
429 deployment). Error bars are scaled to a tenth of hourly variances over the deployment month.
430 The yellow sun symbol indicates mid-day in local time. CC: cross-correlation coefficient at zero
431 delay.

432

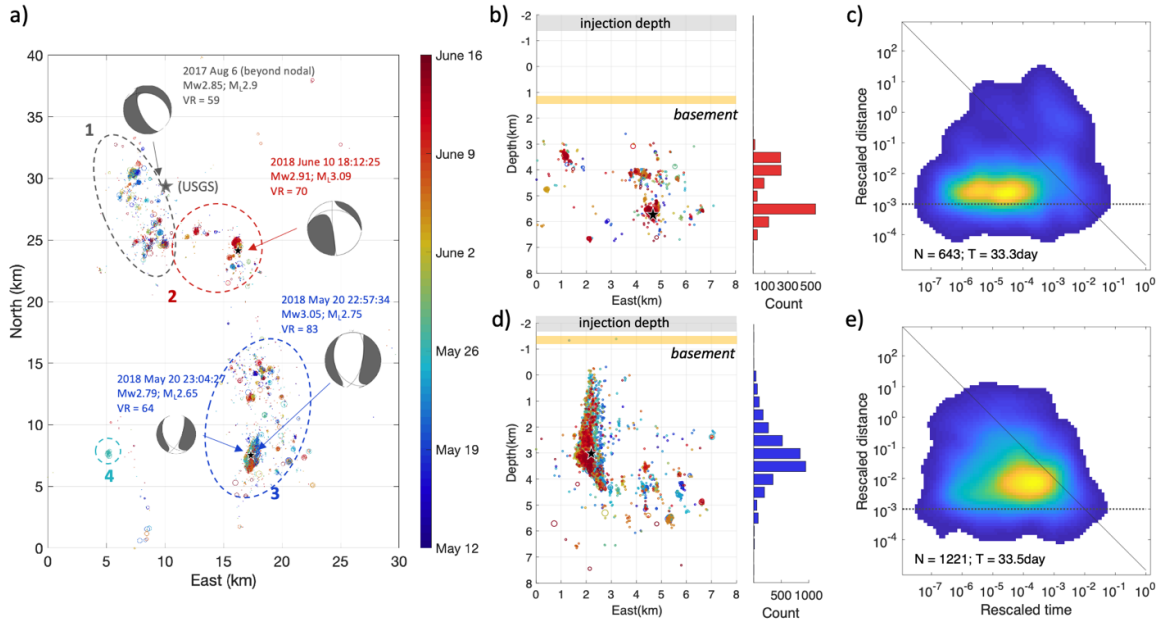

433

434 **Figure 4.** Fault zone characterization. a) Map view of earthquakes colored by dates and
435 moment tensor solutions. The figure presented in kilometers by setting the minimum latitude
436 and longitude of detected events as the SE corner. b) & d) depth view from the south side of
437 cluster 2 and 3, respectively. Basement depths are estimated from Weingarten, (2015). The
438 mainshocks are marked with the black stars. c) & e) Time and space component distribution for
439 the nearest-neighbor distances (Zaliaplin and Ben Zion, 2013) of clusters 2 and 3, respectively.
440 The horizontal dotted line marks a rescaled distance of 10^{-3} and the diagonal represent a
441 stationary (i.e., Poisson) behavior with rescaled distance*rescaled time equal to a constant (i.e.,
442 3).